Journal of Water Process Engineering 78 (2025) 108757

Contents lists available at ScienceDirect

Journal of Water Process Engineering

journal homepage: www.elsevier.com/locate/jwpe

Enhanced electrochemical detection of the antibiotic levofloxacin using temperature optimized Er_2MoO_6 nanomaterials for environmental monitoring

Kumar Gokulkumar [a], Sri Balaji Natarajan [b], Shen-Ming Chen [b,*], Sakthivel Kogularasu [c,d,e], Shih-Hsuan Chen [a], Kun-Mu Lee [a,f,g,h,**]

[a] Department of Chemical and Materials Engineering, Chang Gung University, Taoyuan, 33302, Taiwan
[b] Department of Chemical Engineering and Biotechnology, National Taipei University of Technology, Taipei City, Taiwan
[c] Super Micro Mass Research and Technology Center, Cheng Shiu University, Kaohsiung, 833301, Taiwan
[d] Center for Environmental Toxin and Emerging-Contaminant Research, Cheng Shiu University, Kaohsiung, 833301, Taiwan
[e] Institute of Environmental Toxin and Emerging-Contaminant, Cheng Shiu University, Kaohsiung, 833301, Taiwan
[f] Center for Sustainability and Energy Technologies, Chang Gung University, Taoyuan, 33302, Taiwan
[g] Division of Neonatology, Department of Pediatrics, Chang Gung Memorial Hospital, Linkou, Taoyuan, 33305, Taiwan
[h] College of Environment and Resources, Ming Chi University of Technology, New Taipei City, 24301, Taiwan

ARTICLE INFO

Editor: Soroush Abolfathi

Keywords:
Nanomaterial
Er_2MoO_6
Rare-earth-based nanoparticles
Environmental samples
Thermal modulation
Electrochemical detection

ABSTRACT

Levofloxacin (LFX) is widely used in healthcare and aquaculture due to its structural stability and physicochemical properties, which allow its residues to persist in the environment and pose significant risks to human health. However, conventional sensors often lack the efficiency and sensitivity required for detecting complex molecular compounds. In this work, a temperature-optimized erbium molybdate (Er_2MoO_6)-based electrochemical sensor was developed for the highly sensitive and selective detection of LFX. The Er_2MoO_6 nanoparticles, synthesized via a hydrothermal process at two different temperatures (160 °C and 200 °C), exhibited excellent stability and reusability for sustained sensing. Notably, the sample (Er_2MoO_6-T2) synthesized at 200 °C demonstrated significant improvements in crystallinity, morphology, and surface properties. The Er_2MoO_6-T2 modified glassy carbon electrode achieved an ultra-low detection limit of 0.00146 μM, a wide linear range (0.0025–2125.5 μM), and outstanding selectivity, reproducibility, and long-term stability. Furthermore, the temperature-optimized Er_2MoO_6 nanoparticles enabled high recovery rates of 98.6 % in complex matrices such as human urine, blood, lake water, and pond water, confirming the sensor's reliability for real-world applications. This study highlights the potential of Er_2MoO_6-based electrodes as high-performance electrochemical platforms for antibiotic monitoring.

1. Introduction

The rapid rise of antibiotic-resistant pathogens is a major global health threat, driven mainly by excessive use and environmental release of antibiotics. These drugs, commonly used in medicine, agriculture, and aquaculture, have led to significant risks for both humans and aquatic ecosystems due to their widespread overuse [1–3]. Fluoroquinolones, synthetic broad-spectrum antibiotics introduced in the 1980s, have become widely used due to their strong antibacterial effectiveness [4]. Levofloxacin (LFX), chemically known as (*S*)-9-fluoro-2,3-dihydro-3-methyl-10-(4-methyl-1-piperazinyl)-7-oxo-7H-pyrido[1,2,3-de]-1,4-benzoxazine-6-carboxylic acid [5–7], is a third-generation fluoroquinolone that is commonly prescribed to treat a range of bacterial infections, including those of the urinary tract, respiratory system, skin, and gastrointestinal tract [4,8,9]. Although fluoroquinolones are quickly absorbed orally, about 87 % is excreted unchanged in urine, causing their lasting presence in sewage and water. Their poor biodegradability further contributes to environmental persistence. [10], can cause serious ecological and health consequences, including antimicrobial resistance and toxic side effects such as colitis, liver and kidney

* Corresponding author.
** Correspondence to: K.-M. Lee, Department of Chemical and Materials Engineering, Chang Gung University, Taoyuan, 33302, Taiwan.
E-mail addresses: smchen78@ms15.hinet.net (S.-M. Chen), kmlee@mail.cgu.edu.tw (K.-M. Lee).

https://doi.org/10.1016/j.jwpe.2025.108757
Received 21 July 2025; Received in revised form 8 September 2025; Accepted 12 September 2025
Available online 18 September 2025

damage, and blood disorders [11–13]. Given the urgent threat posed by LFX contamination, developing sensitive and selective detection methods is essential for timely analysis and effective monitoring of public health and the environment.

Traditional methods like HPLC, GC–MS, and fluorescence spectroscopy are accurate but costly, complex, and need extensive sample preparation. [14,15]. In contrast, electrochemical sensing platforms have gained considerable attention due to their inherent advantages, including rapid response, miniaturization potential, low detection limits, and high selectivity. The performance of these sensors is highly influenced by the choice and design of electrode modifiers, particularly nanostructured materials with tailored surface properties. [16–19]

Although numerous electrochemical sensors have been developed for LFX detection, many are based on carbon nanomaterials, metal oxides, other composites, which often suffer from limited sensitivity, narrow linear ranges, and poor long-term stability. Recently, rare-earth molybdates (RE_2MoO_6) have gained significant attention due to their high chemical stability, rich electronic states, and tunable lattice structures, making them highly promising for electrochemical sensing applications. Molybdates, as a versatile class of rare-earth-containing materials, exhibit multifunctional properties and find broad applications in electrochemical sensors, photocatalysis, photonic devices, and solid-state lasers, underscoring their potential for advanced functional material design. [20].Er_2MoO_6 have recently attracted attention for their unique spectroscopic and electronic properties, stemming from rare-earth ions in low-symmetry lattice sites. Combined with molybdenum's redox activity, these features make them promising for high-performance electrochemical applications. [21]. In this study, erbium molybdate (Er_2MoO_6) nanoparticles were synthesized hydrothermally at two temperatures, 160 °C (T1) and 200 °C (T2), to investigate how heat affects their physical and electrochemical properties. In this context, we hypothesize that temperature-driven crystallographic engineering of Er_2MoO_6 nanostructures can directly influence electron transfer kinetics and enhance LFX oxidation. Higher synthesis temperatures are expected to improve crystallinity, lattice ordering, and polyhedral connectivity, resulting in reduced defect density, better charge mobility, and faster interfacial electron transport. This structural optimization is anticipated to yield superior electrocatalytic activity compared to conventional LFX sensors and previously reported rare-earth molybdate systems. The materials were characterized by SEM, XRD, FTIR, Raman, TEM, and XPS, revealing that higher temperature improved crystallinity, created a more uniform structure, and increased electroactive surface sites. When used to modify glassy carbon electrodes, the T2 sample showed better current response, lower charge-transfer resistance, and clearer redox peaks. These enhancements are linked to the larger electroactive surface area and improved charge transport from the higher-temperature synthesis, This temperature optimization highlights a rational design approach, showing how heat directly controls the crystal structure defect landscape, and electrochemical behavior of the sensing material. [22] The elevated temperature promotes controlled nucleation and growth, leading to a reduction in grain boundary resistance, enhancement in crystallographic order [23,24], and the formation of beneficial oxygen vacancies or surface defects [25,26], which together contribute to improved analyte adsorption and electron transfer kinetics [27]. Overall, this study highlights how synthesis temperature tunes the electrocatalytic activity of Er_2MoO_6, showcasing its potential for sensor applications.

This study pioneers a temperature-optimized synthesis approach for Er_2MoO_6 nanostructures, establishing a clear structure–function relationship that directly enhances their electrochemical performance. [28–30]. Unlike conventional methods, this dual-temperature strategy offers precise control over material properties, resulting in an innovative sensing platform for levofloxacin detection. [31–34]. The fabricated sensor demonstrated an exceptionally wide linear range (0.0025–2125.50 μM), an ultralow detection limit of 0.00146 μM, and a high sensitivity of 1.36 μA μM^{-1} cm^{-2}, outperforming existing LFX sensors. Furthermore, validation with real samples, including human blood, urine, and environmental water, yielded an impressive recovery rate of ~98.6 %, confirming its reliability and robustness for practical use. These findings not only highlight the novelty of temperature-controlled nanostructure engineering but also establish a scalable and cost-effective platform for pharmaceutical contaminant monitoring. This work provides a foundation for extending the concept to other metal oxides and integrating the sensor into portable, point-of-care devices for clinical and environmental applications.

2. Chemicals and methods

All chemicals used in this study were of analytical grade and purchased from Sigma-Aldrich. They were used without any further purification to ensure reproducibility and consistency in experimental results. Detailed information regarding the specific chemicals, buffer solution preparation, experimental conditions, and instrumentation is provided in Supplementary **Sections S1–S3** for better clarity and transparency. Additionally, the operational details for some of the characterization techniques, including the instrumental settings, measurement parameters, and data acquisition procedures, are described in the related literature. [35–37]

2.1. Synthesis of Er_2MoO_6 nanostructures via hydrothermal method at two temperatures

Er_2MoO_6 nanoparticles were synthesized using a modified hydrothermal method, as illustrated in Fig. 1, with erbium nitrate hexahydrate ($Er(NO_3)_3{\cdot}6H_2O$) and disodium molybdate dihydrate ($Na_2MoO_4{\cdot}2H_2O$) as precursor materials. First, 0.02 M $Er(NO_3)_3{\cdot}6H_2O$ was dissolved in a mixed solvent of 80 mL ethanol and 20 mL ethylene glycol (EG) and sonicated for 10 min to ensure complete dissolution. Meanwhile, 0.01 M $Na_2MoO_4{\cdot}2H_2O$ was dissolved in 50 mL of doubly distilled water with continuous stirring until a clear solution formed. The molybdate solution was then added dropwise to the Er^{3+} solution under vigorous stirring.

Next, 1 M NaOH was added dropwise to adjust the pH to 9, facilitating the controlled precipitation of Er—Mo hydroxide complexes. The resulting suspension was transferred into a 100 mL Teflon-lined stainless-steel autoclave and subjected to hydrothermal treatment at two temperatures: 160 °C (T1) and 200 °C (T2), each for 12 h. After naturally cooling to room temperature, the precipitates were collected by centrifugation, thoroughly washed several times with distilled water and ethanol, and dried overnight under vacuum at 60 °C. The final products, labelled Er_2MoO_6-T1 and Er_2MoO_6-T2, correspond to the samples synthesized at 160 °C and 200 °C, respectively. These materials were then comprehensively characterized for their physicochemical properties and evaluated for electrochemical performance.

2.2. Preparation of Er_2MoO_6 catalyst

Catalyst inks were prepared by dispersing 2 mg of the synthesized Er_2MoO_6 samples (Er_2MoO_6_T1 and Er_2MoO_6-T2) separately in 3 mL of deionized water, followed by ultrasonication for 30 min to obtain a uniform and stable suspension. A 6 μL aliquot of the homogeneous ink was then drop-cast onto pre-polished glassy carbon electrodes (GCEs). The modified electrodes were dried at 60 °**C** to ensure firm adhesion and were subsequently used for electrochemical measurements.

2.3. Electrode fabrication

Before modification, the GCE was carefully polished with 0.05 μm alumina slurry until it had a mirror-like finish. This step removed impurities and ensured a clean surface, which is essential for efficient electron transfer and improved sensor performance. After polishing, the electrode was thoroughly rinsed with deionized water and gently dried

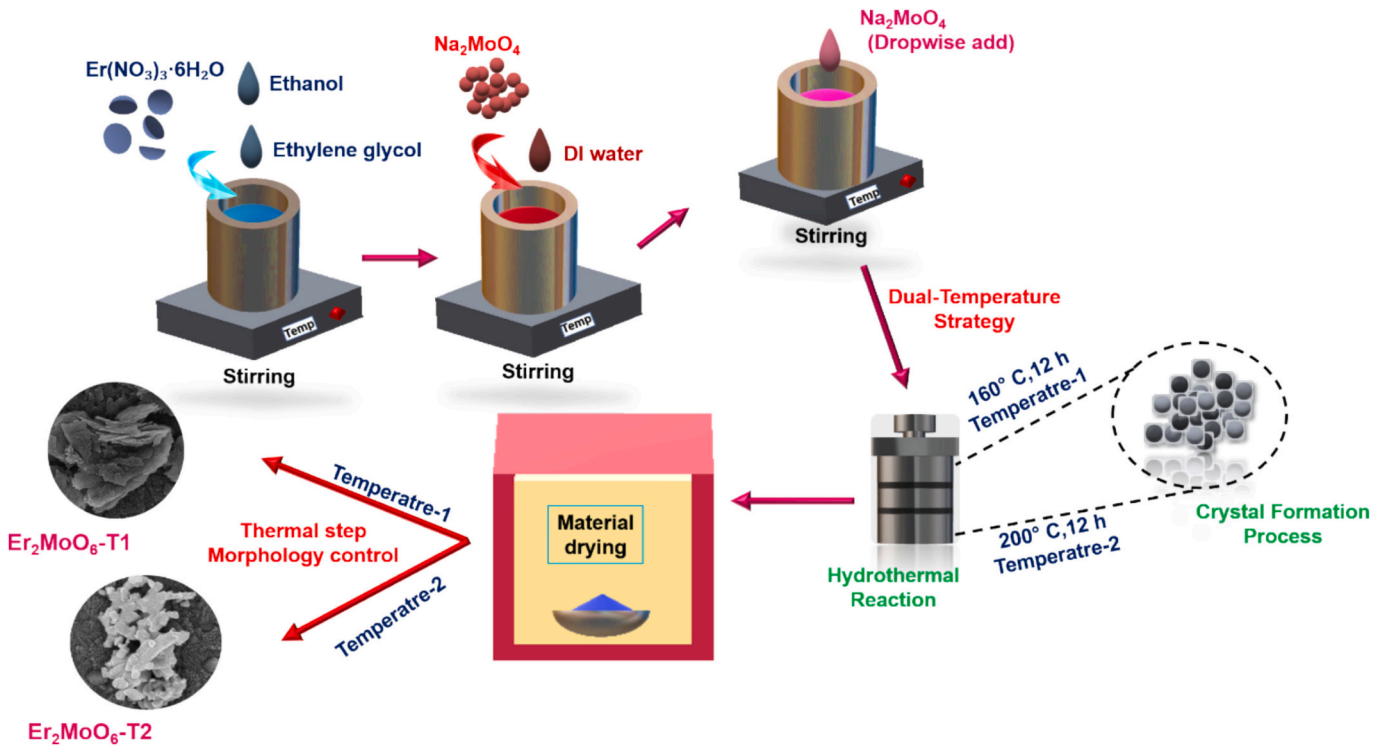

Fig. 1. Illustration of the hydrothermal preparation of Er_2MoO_6 nanoparticles under two temperature conditions.

under a nitrogen stream.

Next, 6 μL of the Er_2MoO_6 dispersion either from the T1 or T2 sample was carefully drop-cast onto the cleaned GCE surface and dried at 60 °C to firmly attach the catalyst layer. [16,38] The modified electrodes, Er_2MoO_6-T1/GCE and Er_2MoO_6-T2/GCE, were then ready for electrochemical testing as illustrated in **Scheme S1**. The electrochemical detection of LFX was carried out using CV and DPV, a standard three-electrode setup was used, consisting of the modified GCE as the working electrode, an Ag/AgCl reference electrode, and a platinum wire counter electrode. Measurements were performed in the potential range of 0.2 to 1.2 V, chosen based on the redox characteristics of LFX.

2.4. Statistical analysis

All electrochemical measurements were performed using three independently fabricated Er_2MoO_6-modified glassy carbon electrodes ($n = 3$) to ensure reproducibility and reliability. For each electrode, three replicate measurements were recorded under identical experimental conditions. The reported values represent the average of three independent experiments, and all data are expressed as mean ± standard deviation (SD). In all relevant figures, including CV, DPV, EIS, optimization studies, and calibration curves, error bars represent the SD calculated from triplicate measurements. This approach ensures that the presented results are statistically robust, reproducible, and suitable for accurate performance evaluation of the proposed sensor.

2.5. Electrochemically active surface area (ECSA) analysis

The electrochemically active surface area (ECSA) of the bare GCE and Er_2MoO_6-modified electrodes (Er_2MoO_6-T1/GCE and Er_2MoO_6-T2/GCE) was calculated using the well-established Randles–Ševčík equation (Eq. 1) based on CV data obtained in a 5 mM $[Fe(CN)_6]^{3-/4-}$ solution containing 0.1 M KCl [39].

$$Ip = \left(2.69 \times 10^5\right) \times n^{3/2} \times A \times D^{1/2} \times C \times v^{1/2} \quad (1)$$

where Ip is the anodic peak current (μA), n is the number of electrons transferred ($n = 1$), A is the electrochemically active surface area (cm^2), D is the diffusion coefficient of $[Fe(CN)_6]^{3-/4-}$ (taken as 7.6×10^{-6} $cm^2 \cdot s^{-1}$), C is the concentration of the redox probe (0.005 M), and v is the scan rate ($V \cdot s^{-1}$). The slope of the linear plot of Ip versus $v^{1/2}$ was used to estimate the ECSA of each electrode.

3. Structural and phase evolution of Er_2MoO_6 temperature-driven crystallographic engineering

3.1. X-ray diffraction (XRD) analysis

To investigate the phase formation and crystallographic changes in Er_2MoO_6 nanoparticles synthesized at different hydrothermal temperatures, X-ray diffraction (XRD) analysis was conducted on both Er_2MoO_6-T1 (160 °C) and Er_2MoO_6-T2 (200 °C) samples. The diffraction patterns, shown in Fig. 2A, reveal well-defined peaks for both samples, indicating a monoclinic crystal structure with C2/c symmetry. These results align well with the standard JCPDS card no. 00–025-0332, confirming the successful formation of the intended phase under both synthesis conditions [40], As shown by the green markers in Fig. 2A, the diffraction peaks at approximately $2\theta = 18.3°$, 28.1°, 30.9°, 35.6°, and 47.2° correspond to the (111), (−202), (−113), (−311), and (−204) planes, confirming the formation of a pure monoclinic Er_2MoO_6 phase. The absence of additional peaks indicates high phase purity with no evidence of secondary phases or unreacted precursors. Notably, the Er_2MoO_6-T2 sample exhibits sharper and more intense peaks, particularly around 30.9°, compared to Er_2MoO_6-T1, suggesting improved crystallinity and larger crystallite size at the higher synthesis temperature. This enhancement arises from better nucleation and grain growth at 200 °C, which promotes superior atomic ordering. Such structural refinement is expected to improve electrical conductivity and enhance catalytic performance. Overall, these results demonstrate that hydrothermal synthesis temperature plays a critical role in determining the structural quality and functional properties of Er_2MoO_6.

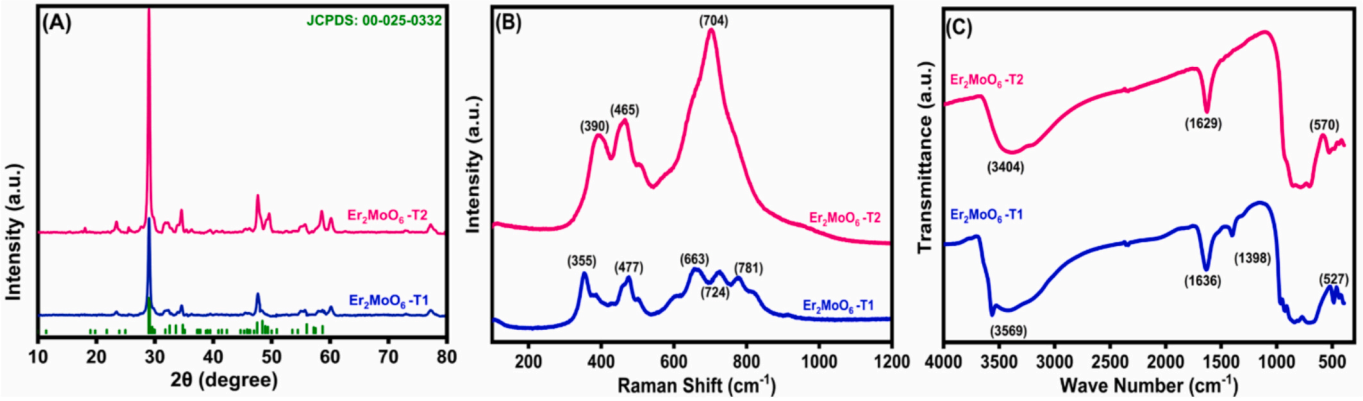

Fig. 2. (A) XRD patterns of Er_2MoO_6–160 °C (T1) and Er_2MoO_6–200 °C (T2), (B) Raman Spectra of Er_2MoO_6–160 °C (T1) and Er_2MoO_6–200 °C (T2) (C) FTIR data of Er_2MoO_6–160 °C (T1) and Er_2MoO_6–200 °C (T2).

3.1.1. Thermal modulation of crystallinity and lattice architecture

The effect of hydrothermal temperature on the crystallinity and lattice structure of Er_2MoO_6 was analysed using XRD. At the lower temperature (T1, 160 °C), the sample showed broad, low-intensity peaks with a high background, indicating nano crystallinity, limited grain growth, and lattice disorder. In contrast, the T2 sample (200 °C) exhibited sharper, more intense peaks with reduced FWHM, confirming enhanced crystallinity, better grain growth, and fewer defects. A slight shift of peaks to lower 2θ angles in T2 suggests lattice expansion caused by strain relaxation and optimized local bonding, resulting in a more ordered monoclinic framework.

Rietveld refinement [41] Consistent with related studies on lanthanide molybdates, both T1 and T2 samples retain monoclinic symmetry (C2/c). However, the refined lattice parameters of the T2 sample show slight but meaningful changes especially in unit cell dimensions and the β angle (~108°)—indicating thermally driven structural reorganization and lattice relaxation.

3.1.2. Lattice geometry and rare-earth-induced ordering

In the monoclinic Er_2MoO_6 structure, Er^{3+} ions occupy three distinct Wyckoff positions (4e, 4e, and 8f), forming a 3D coordination network that defines the lattice geometry and structural order. At the higher synthesis temperature (T2), the improved crystallinity facilitates the formation of well-organized RE–O–RE (rare-earth–oxygen–rare-earth) chains, such as I-type and III-type, which are commonly observed in similar molybdate frameworks. [42], These chains become more defined under elevated temperatures due to reduced lattice strain, lower oxygen distortion, and enhanced symmetry. This shift from the disordered T1 phase to the ordered T2 phase reflects a deeper structural reorganization that influences electronic structure and vibrational dynamics. As confirmed by EIS and CV, these atomic-scale improvements at T2 enhance charge transport and redox activity, underscoring the importance of rare-earth site ordering in optimizing the electrochemical performance of molybdate-based materials.

3.2. Raman spectroscopic analysis

Raman spectroscopy was employed to investigate the local vibrational properties, lattice dynamics, and structural integrity of the Er_2MoO_6 samples synthesized at 160 °C (T1) and 200 °C (T2), as shown in Fig. 2B. The T1 sample exhibits broad and low-intensity bands in the 350–900 cm^{-1} range, with characteristic peaks at approximately 390, 465, 663, 724, and 781 cm^{-1}, which are associated with the bending and stretching vibrations of Mo—O bonds within distorted MoO_6 octahedra. The pronounced spectral broadening, overlapping features, and lower intensities indicate significant structural disorder, poor octahedral connectivity, and high defect density caused by limited thermal energy during low-temperature synthesis.

In contrast, the T2 sample synthesized at 200 °C demonstrates sharper, more intense, and well-resolved peaks at 355, 477, 540, 704, and 800 cm^{-1}, indicating improved crystallinity, stronger metal–oxygen bonding, and reduced vibrational disorder. Notably, the observed red-shifts in certain key Raman bands from 390 to 355 cm^{-1} and 465 to 477 cm^{-1} suggest a relaxation of internal strain and a more stable Mo—O bonding environment at higher synthesis temperatures. Additionally, several high-frequency peaks seen in T1 converge into a single, well-defined band at 704 cm^{-1} for T2, indicating a transition from a disordered to a more symmetrical and uniform MoO_6 framework. These results confirm that hydrothermal temperature plays a crucial role in modulating the phonon behavior and lattice ordering of Er_2MoO_6. The improved vibrational coherence and stronger Mo—O coupling in T2 correlate directly with the enhanced electronic conductivity and faster charge-transfer kinetics observed in electrochemical studies. Thus, Raman analysis provides compelling evidence that temperature-driven crystallographic tuning leads to a more stable, well-ordered lattice, which underpins the superior sensing performance of the Er_2MoO_6–T2/GCE electrode. [43].

3.3. FTIR analysis

FTIR spectroscopy was performed to investigate the local bonding environments and structural changes in Er_2MoO_6 nanoparticles synthesized at 160 °C (T1) and 200 °C (T2), as shown in Fig. 2C. The T1 sample exhibits broad, low-intensity bands in the regions of approximately 820–880 cm^{-1} and 450–550 cm^{-1}, which correspond to the Mo—O stretching vibrations within the MoO_6 octahedra and the Er—O vibrations, respectively. The broadness and low resolution of these peaks suggest incomplete formation of MoO_6 and ErO polyhedral, indicating a disordered structure with local lattice distortions and poor polyhedral connectivity. Additionally, the T1 sample shows broad absorptions in the 1600–3500 cm^{-1} region, which are attributed to surface hydroxyl groups and adsorbed water molecules, further confirming a defect-rich and hydrophilic surface. In contrast, the T2 sample exhibits sharper and more intense peaks with reduced hydroxyl-related absorptions, implying better polyhedral ordering, stronger metal–oxygen interactions, and enhanced structural stability at higher synthesis temperatures. [44]. In contrast, the T2 sample exhibits sharper and more intense bands with a blue shift in the Mo—O stretching region, indicating stronger bonding and improved lattice order. The diminished low-frequency shoulders and hydroxyl-related bands confirm reduced defects and dehydration. These results suggest that higher thermal energy promotes better atomic packing and polyhedral connectivity, leading to enhanced structural rigidity. Such improvements are expected to support better charge transport and overall electrochemical

performance.

3.4. Morphological evolution and nanostructure development SEM analysis

To explore the influence of hydrothermal temperature on the microstructure of Er_2MoO_6, SEM imaging was carried out Fig. 3 **A-C**. At 160 °C (T1), the material displays irregular, loosely packed flake-like structures with poor interconnectivity and blurred grain boundaries signs of limited atomic mobility and a kinetically hindered growth process. This disordered morphology, associated with high defect density and incomplete grain development, often results in poor electrical conductivity and sluggish electrochemical kinetics due to inefficient charge transport pathways. Fig. 3**D—F** In contrast, the sample synthesized at 200 °C (T2) reveals a highly organized, porous nanosheet network with interwoven lamellar structures. This morphology reflects a temperature-induced boost in crystallite assembly, where enhanced thermal energy enables atom diffusion, grain boundary movement, and anisotropic growth. Mechanisms such as Ostwald ripening and oriented attachment contribute to the formation of larger, more stable crystalline domains with uniform pore distribution.

The improved structural integrity and hierarchical porosity at T2 not only enhance electrolyte penetration and active surface area but also support faster ion diffusion and more efficient electron percolation. This well-connected framework reduces charge resistance and stabilizes the electrode–electrolyte interface, leading to reproducible and higher redox performance. Thus, the thermally engineered microstructure at T2 is not just a byproduct of synthesis but a critical design element that directly improves electrochemical sensing behavior.

3.4.1. Elemental mapping

To verify the elemental composition and spatial uniformity of Er_2MoO_6 synthesized at 200 °C (T2), EDS elemental mapping was performed Figs. 3**G–I.** The maps show a uniform distribution of Er, Mo, and O across the sample, confirming successful incorporation of all elements without signs of phase segregation or clustering. This homogeneity suggests complete precursor conversion and strong atomic level integration, driven by the optimized thermal conditions. Such uniform composition is essential for stable electrochemical performance, as it ensures consistent charge transfer across the surface, reduces redox variability, and enhances sensor reproducibility.

3.5. X-ray photoelectron spectroscopy (XPS) analysis

X-ray photoelectron spectroscopy (XPS) was conducted on the Er_2MoO_6 sample synthesized at 200 °C (T2) to analyze its surface chemistry and electronic states Fig. 4A–C**.** Previous XRD and SEM analyses identified Er_2MoO_6–T2 as the optimal material due to its superior crystallinity and uniform nanosheet morphology, and the XPS results further confirm these findings. The Er 4d spectrum Fig. 4A shows a sharp, well-defined peak at ~168.5 eV, confirming the presence of the trivalent Er^{3+} oxidation state with a stable, defect-minimized local environment. The Mo 3d spectrum Fig. 4B displays two prominent peaks at ~232.4 eV and ~ 235.6 eV, corresponding to Mo $3d_{5/2}$ and Mo $3d_{3/2}$, respectively, which are characteristic of the fully oxidized Mo^{6+} state. The absence of additional low-binding-energy peaks suggests that the MoO_6 octahedra are well-coordinated and free from significant defect-induced states, indicating strong structural stability.

The O 1 s spectrum Fig. 4C reveals a dominant peak at ~529.6 eV, assigned to lattice oxygen, along with a minor shoulder at ~531.2 eV, attributed to surface hydroxyl groups and/or oxygen vacancies. These limited oxygen-related defects in Er_2MoO_6–T2 can introduce electron-rich active sites, thereby enhance electron transfer and improve the electrocatalytic performance toward LFX oxidation. The relatively low fraction of hydroxyl species compared to lattice oxygen also indicates better dehydration and a more ordered lattice framework, which aligns with the improved crystallinity observed in XRD and SEM analyses [45]. These surface chemical features are crucial as they directly impact the redox behavior and electron transfer efficiency of the material. The minimal surface defects and strong metal–oxygen bonding contribute to the material's electrochemical stability and durability. Such a well-defined electronic structure is expected to promote consistent sensor responses and improved charge carrier mobility. Overall, the XPS data confirm a stoichiometric, chemically stable Er_2MoO_6 with well-defined

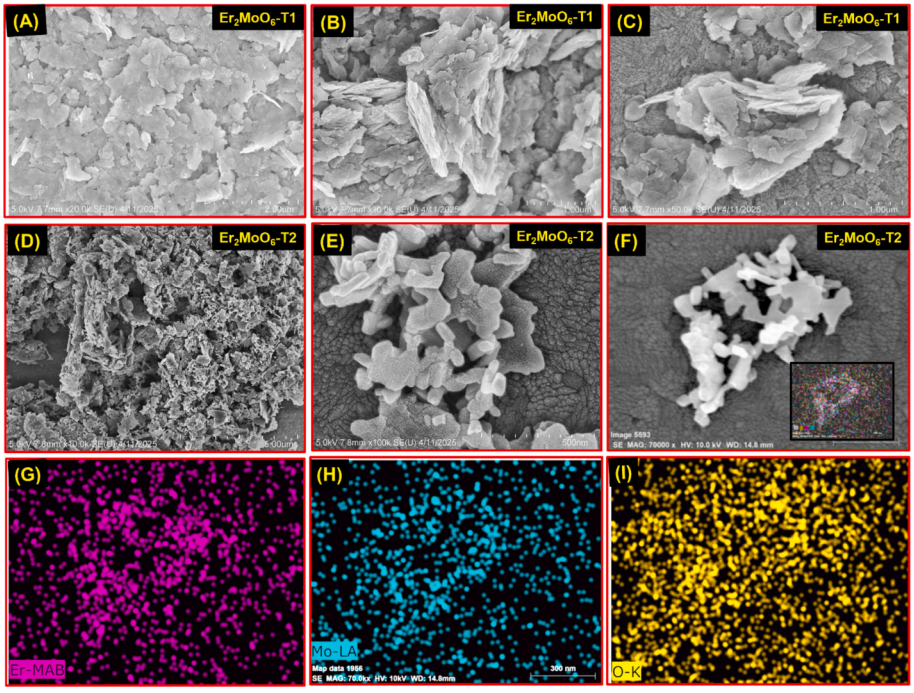

Fig. 3. (A–C) SEM images of Er_2MoO_6 synthesized at 160 °C (T1) at different magnifications; (E–F) SEM images of Er_2MoO_6 synthesized at 200 °C (T2) at different magnifications; (G–I) Elemental mapping analysis of Er_2MoO_6–200 °C (T2), showing the uniform distribution of constituent elements.

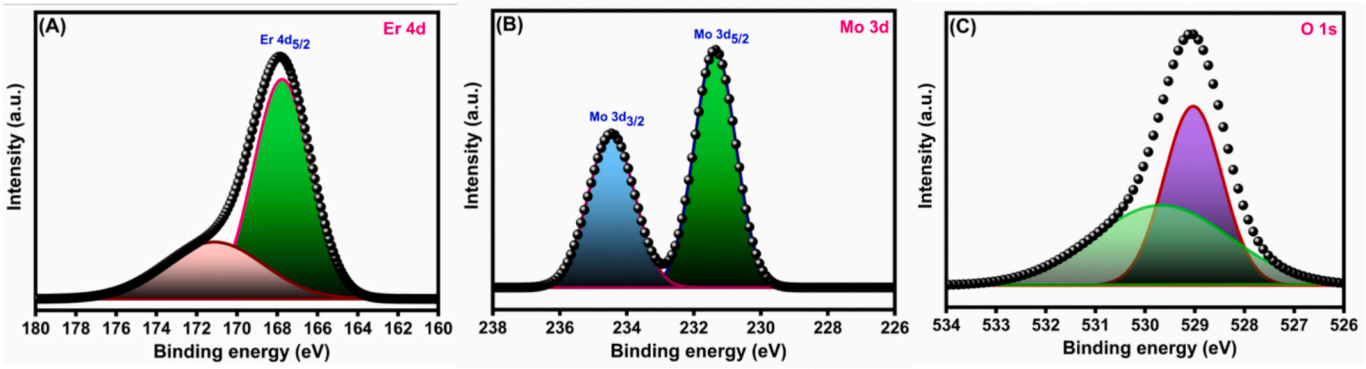

Fig. 4. XPS spectra of Er_2MoO_6 synthesized at 200 °C (T2): (A) high-resolution spectrum of Er 4d, (B) high-resolution spectrum of Mo 3d, and (C) high-resolution spectrum of O 1 s.

oxidation states and minimal surface disorder, supporting its robust electrochemical performance.

3.6. Nanoscale structural characterization TEM analysis

TEM was employed to gain deeper insight into the internal nanostructure of the Er_2MoO_6 material synthesized at Er_2MoO_6–200 °C (T2), which was selected for advanced characterization due to its superior performance confirmed by SEM and electrochemical analyses. The TEM images presented in Fig. 5 provide a multiscale visualization of the material, revealing how temperature-driven synthesis influences hierarchical organization from the microscale down to the atomic level.

3.6.1. Multiscale TEM imaging of Temperature-2 synthesized sample

Fig. 5A, taken at low magnification, provides a broad view of the Er_2MoO_6 morphology, revealing well-dispersed, interconnected nanosheet-like domains alongside some aggregated areas. This overview highlights the successful formation of a porous framework, crucial for efficient mass transport in electrochemical applications. At intermediate magnification, Fig. 5B zooms in on particle clusters, showing fairly uniform crystallite sizes and improved grain connectivity, which supports continuous electron pathways. These features reflect a thermal synthesis approach that fosters compact yet electrochemically accessible nanostructures. Fig. 5C offers a closer look, displaying densely packed nano crystallites with no signs of phase segregation or amorphous material, underscoring the uniformity achieved under optimized thermal conditions. Fig. 5D focuses on the nanoflake edges, revealing sharp boundaries and distinct contrast variations that indicate thin, well-faceted crystallites with minimal distortion. These well-defined edges enhance surface area and provide reactive sites vital for electrochemical activity. Importantly, the hierarchical self-assembly of nanosheets into a three-dimensional porous network suggests that the 200 °C hydrothermal synthesis encourages controlled nucleation and kinetically favorable crystal growth, enabling reproducible and scalable morphology.

3.6.2. Crystallinity and structural coherence confirmed by HRTEM and SAED

HRTEM images in Fig. 5E show clear, continuous lattice fringes, indicating high crystallinity. The measured spacing (~0.220 nm) matches the (hkl) planes from XRD, confirming the monoclinic phase and atomic-level ordering achieved at the higher synthesis temperature. Uniform fringes suggest minimal strain or defects, demonstrating a well-ordered crystal structure. The SAED pattern Fig. 5F displays sharp diffraction spots in concentric rings, confirming a polycrystalline material with uniformly oriented nanocrystals and excellent thermal stability. These TEM results highlight how increased synthesis temperature improves both macroscopic structure and nanoscale ordering. The interconnected nanoflakes, sharp edges, and aligned lattice fringes create an optimized architecture that enhances electrochemical performance. Er_2MoO_6 synthesized at 200 °C (T2) thus offers a high-quality, scalable, and eco-friendly material for advanced sensing applications without requiring high-temperature calcination.

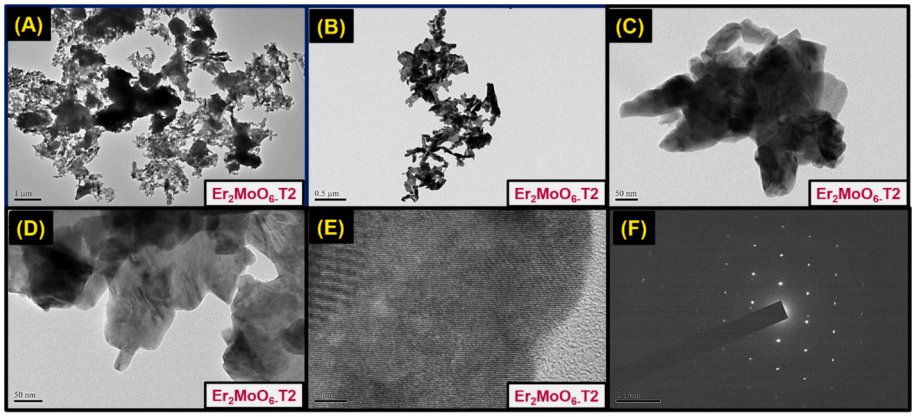

Fig. 5. TEM characterization of Er_2MoO_6 synthesized at 200 °C (T2)
(A–D) TEM images at different magnifications showing the formation of well-defined nanosheet-like structures with uniform morphology and interconnected domains.
(E) High-resolution TEM (HRTEM) image revealing clear lattice fringes with an interplanar spacing of ~0.220 nm, corresponding to the (hkl) plane, confirming the high crystallinity of the material. (F) Selected area electron diffraction (SAED) pattern displaying distinct and sharp diffraction spots, indicating a polycrystalline nature with uniformly oriented nanocrystals.

3.7. EIS analysis

Electrochemical impedance spectroscopy (EIS) was employed to evaluate the interfacial electron transfer behavior of bare GCE, Er_2MoO_6–T1/GCE, and Er_2MoO_6–T2/GCE in a standard redox probe solution containing 5 mM $[Fe(CN)_6]^{3-/4-}$ in 0.1 M KCl. The Nyquist plots shown in Fig. 6A reveal that the bare GCE has the largest semicircle, corresponding to a high charge transfer resistance (Rct ≈ 500 Ω·cm^2). This is due to the poor conductivity and sluggish electron kinetics of the unmodified electrode surface. Upon modification with Er_2MoO_6–T1, the semicircle diameter decreases significantly, reducing Rct to approximately 280 Ω·cm^2. This improvement is attributed to the increased surface roughness, enhanced active sites, and better electronic conductivity offered by the nanostructured Er_2MoO_6.

Notably, the Er_2MoO_6–T2-modified electrode exhibits the smallest semicircle with an Rct value around 210 Ω·cm^2, indicating the most efficient electron transfer among the three electrodes, where the bar diagram clearly shows in Fig. 6B. This superior performance is linked to the enhanced crystallinity, reduced grain boundary resistance, and the hierarchical porous nanoflake structure of the T2 sample, which collectively facilitate faster charge transport and improved ion diffusion at the interface. The larger electrochemically active surface area also promotes enhanced interaction with the redox probe. The EIS data were fitted using the Randles equivalent circuit model, incorporating solution resistance (Rs), charge transfer resistance (R_{ct}), double-layer capacitance (C_{dl}), and Warburg impedance (Z_w). As summarized in **Table S1,** the Cdl values increased progressively from bare GCE to Er_2MoO_6–T2/GCE, further confirming the enlarged active surface area and improved capacitive behavior at the electrode–electrolyte interface.

In summary, the EIS results clearly demonstrate that increasing the synthesis temperature of Er_2MoO_6 significantly enhances interfacial charge transfer kinetics and electrochemical accessibility. The improved microstructure and surface properties of the T2 sample make it the optimal choice for achieving high sensitivity and fast response in electrochemical sensing applications.

3.7.1. Cyclic voltammetry analysis

CV was conducted using the redox couple $[Fe(CN)_6]^{3-/4-}$ in 0.1 M KCl to investigate the electrochemical behavior and active surface areas of the bare and modified GCEs. As illustrated in Fig. 6**C**, the bare GCE shows broad and low-intensity redox peaks, indicating sluggish electron transfer and a limited electroactive surface. Upon modification with Er_2MoO_6–T1, a notable increase in peak currents and a reduced peak-to-peak separation ΔE_p were observed Fig. 6D, suggesting improved electron transfer kinetics due to enhanced surface conductivity and the presence of conductive nanostructures. This enhancement is attributed to the moderate thermal treatment at T1, which likely increases the number of active sites without major changes to particle morphology.

Remarkably, the Er_2MoO_6–T2-modified GCE exhibits the highest redox peak currents and the smallest ΔE_p, as seen in Fig. 6E and further supported by Fig. 6F. These results reflect highly efficient charge transfer behavior, attributed to the optimized synthesis conditions at T2, which enhance crystallinity, particle connectivity, and porosity factors that collectively improve ion diffusion and electron transport. To gain further insight into the redox mechanism, scan rate-dependent CV studies were performed between 20 and 300 mV/s. For Er_2MoO_6–T1/GCE, the CV curves in Fig. 6G show a proportional increase in peak currents with increasing scan rate, maintaining quasi-reversible behavior. The corresponding plots of peak current versus the square root of scan rate Fig. 6H display strong linearity $R^2 = 0.9994$ for anodic and 0.9933 for cathodic peaks, indicating a diffusion-controlled redox process. Similarly, Er_2MoO_6–T2/GCE demonstrates increased peak currents with scan rate Fig. 6I, and the linear relationships **in** Fig. 6J $R^2 = 0.9988$ and 0.9903 further confirm a diffusion-limited mechanism. Notably, the steeper slope observed for T2 signifies a higher electron transfer rate and greater electroactive surface area than T1.

To quantitatively evaluate these enhancements, the anodic peak current (μA), ΔE_p (mV), and electroactive surface area (cm^2) for all three electrodes were calculated using the Randles–Sevcik equation **Eq. 1**, with the results summarized in **Table S2**. These findings demonstrate that the Er_2MoO_6–T2/GCE achieves a 2.7-fold increase in electroactive surface area compared to the bare GCE, and offers approximately 36 % improvement over the T1-modified electrode. This significant enhancement highlights its strong potential for use in high-sensitivity electrochemical sensing applications.

3.8. Proposed electrochemical oxidation mechanism of LFX

The electrochemical behavior of LFX on Er_2MoO_6-modified electrodes suggests a redox mechanism primarily involving the piperazinyl moiety. Upon applying potential, nitrogen atoms in the piperazine ring undergo oxidation, forming a radical cation that further deprotonates

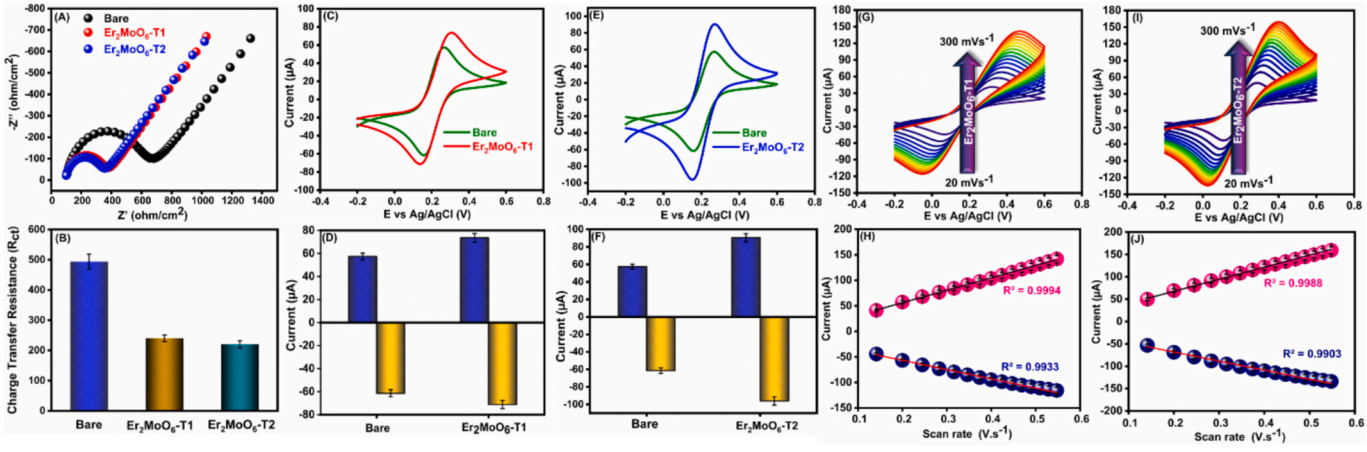

Fig. 6. Electrochemical characterization of bare and modified electrodes. (A) EIS spectra of bare GCE, Er_2MoO_6-T1/GCE, and Er_2MoO_6–T2/GCE recorded in 5 mM $[Fe(CN)_6]^{3-/4-}$ containing 0.1 M KCl. (B) The corresponding Nyquist plots derived from (A) highlight the reduced charge-transfer resistance for Er_2MoO_6–T2/GCE compared to T1 and bare GCE. (C) CV profiles of bare GCE and Er_2MoO_6–T1/GCE in 5 mM $[Fe(CN)_6]^{3-/4-}$ with 0.1 M KCl, and (D) the corresponding current–potential plot obtained from (C). (E) CV profiles of bare GCE and Er_2MoO_6–T2/GCE under similar conditions, with (F) the corresponding current–potential plot derived from (E). (G) CV responses of Er_2MoO_6–T1/GCE at scan rates ranging from 20 to 300 mV·s^{-1}, with (H) the linear relationship between peak current and the square root of scan rate. (I) CV responses of Er_2MoO_6–T2/GCE at scan rates from 20 to 300 mV·s^{-1}, and (J) the corresponding linear plot of peak current versus the square root of scan rate.

and oxidizes into stable products. The Er_2MoO_6 surface enhances this reaction by improving electron transfer and adsorption. This process likely follows a two-electron, two-proton pathway involving sequential electron–proton exchanges. For reductive processes, reactions may initiate at the nitro group, producing a hydroxylamine intermediate through stepwise reduction. [46]. **Scheme S2** illustrates the proposed mechanism and highlights the role of the Er_2MoO_6–T2/GCE in facilitating efficient charge transfer during LFX detection.

3.9. Electrochemical sensing of LFX and optimization of operational parameters

3.9.1. Effect of electrode modification

CV was used to evaluate the electrochemical performance of bare GCE, Er_2MoO_6-T1/GCE, and Er_2MoO_6-T2/GCE in 0.1 M PBS (pH 7.0) containing 100 μM LFX. As shown in Fig. 7A, the bare GCE showed a weak anodic signal due to its limited active surface area and slow electron transfer. Modification with Er_2MoO_6 synthesized at T1 resulted in moderate improvement, attributed to enhanced conductivity and surface activity. In contrast, Er_2MoO_6-T2/GCE exhibited a significantly higher current response, nearly 2.7 times greater than the bare electrode, highlighting the strong impact of synthesis temperature on material performance. The higher temperature improved crystallinity, phase purity, and surface porosity Fig. 7B, creating more electroactive sites and efficient charge transfer pathways. These structural benefits, supported by SEM and XRD analyses, allowed faster LFX diffusion and sharper redox signals. The improved conductivity and nanoscale architecture of Temp-2 material make it an ideal Material for sensitive electrochemical detection. Based on this performance, Er_2MoO_6-T2 was selected for subsequent studies.

3.9.2. Effect of Er_2MoO_6–T2 Electrocatalyst loading on electrode performance

To optimize the sensing performance of the Er_2MoO_6–T2-modified GCE, different volumes (2, 4, 6, and 8 μL) of a 1 mg/mL suspension were drop-cast on the electrode surface, and their CV responses were evaluated. As shown in Fig. 7C, the anodic peak current increased from 2 to 6 μL, indicating better electron transfer and greater surface coverage of active material. This improvement is due to the enhanced electroactive area and availability of catalytic sites provided by the well-structured T2 phase. However, at 8 μL, the current declined, likely a result of excessive film thickness, which restricts mass transport and slows electron transfer. Thick layers may also crack or detach during drying, reducing sensor efficiency. As illustrated in **Fig. 7D**, 6 μL was found to be the optimal loading, offering a well-adhered, porous, and conductive film that ensures efficient analyte interaction. These findings highlight the importance of precise material loading to fully exploit the structural and electronic benefits of Er_2MoO_6–T2 for high-performance electrochemical sensing.

3.9.3. Effect of pH on electrochemical detection of LFX

To optimize the sensing conditions for LFX, the effect of electrolyte pH on its electrochemical behavior was investigated using the Er_2MoO_6–T2-modified GCE, chosen for its superior sensitivity. CV measurements were carried out in 0.1 M PBS, 100 μM of LFX across a pH range of 3 to 11 at a scan rate of 0.05 $V{\cdot}s^{-1}$ Fig. 7E. The results show a strong pH dependence, indicating a proton-coupled electron transfer (PCET) mechanism. In acidic media (pH 3–5), a clear anodic peak was observed, facilitated by abundant H^+ ions that promote protonation of LFX and stabilize its oxidized intermediates. The peak current reached a maximum at pH 7, where LFX exists mostly in a zwitterionic form, favoring interaction with the Er_2MoO_6–T2 surface. The material's high porosity and conductivity further enhance charge transfer and analyte

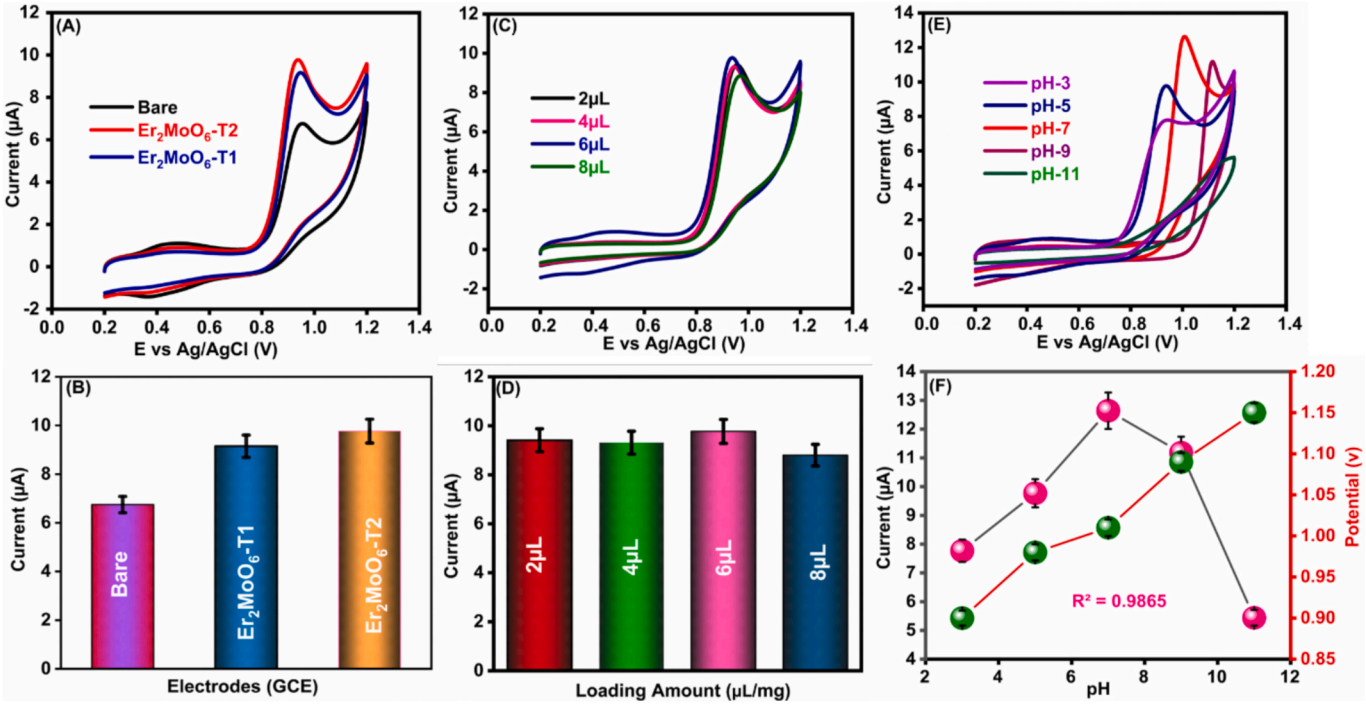

Fig. 7. Electrochemical performance evaluation of bare and modified electrodes toward LFX detection. (A) CV profiles of bare GCE, Er_2MoO_6–T1/GCE, and Er_2MoO_6–T2/GCE recorded in 100 μM LFX solution, showing a significantly enhanced electrochemical response for the modified electrodes, particularly Er_2MoO_6–T2/GCE. (B) Comparison of peak current responses for bare and modified electrodes, demonstrating the superior sensitivity of the T2-modified electrode. (C) CV responses of Er_2MoO_6–T2/GCE with different loading amounts of the Er_2MoO_6 composite, showing the effect of catalyst content on electrochemical activity. (D) Corresponding calibration plot derived from (C), illustrating the influence of composite loading on sensor performance. (E) CV profiles of Er_2MoO_6–T2/GCE recorded at varying pH values ranging from 3 to 11, highlighting the impact of solution pH on sensing behavior. (F) Plot of peak current versus pH, indicating the optimal pH condition for achieving maximum sensor response.

adsorption. At alkaline pH (9–11), a gradual drop in current was seen due to deprotonation of LFX and active sites, impairing PCET and reducing surface interaction. Additionally, the anodic peak shifted negatively with increasing pH, confirming the involvement of protons in the redox reaction. These observations support a two-electron, two-proton mechanism likely starting with nitro group reduction and stepwise protonation to form a hydroxylamine intermediate. Overall, pH 7 was found to be optimal for effective electrochemical detection of LFX.

3.9.4. Proposed electrochemical mechanism of LFX oxidation

The possible electrochemical mechanism is derived from eqs. 2 to 5.

Step 1: One-electron oxidation of secondary amine.

$$LFX - NH - \rightarrow LFX - N\bullet \quad (2)$$

Step 2: Proton loss

$$LFX - N\bullet \rightarrow LFX - N: \quad (3)$$

Step 3: Second one-electron oxidation.

$$LFX - N: \rightarrow LFX - N^{+} = \quad (4)$$

Step 4: Protonation or water attack.

$$LFX - N^{+} = +H_2O \rightarrow LFX - NH(OH) \quad (5)$$

Where represents the LFX is Levofloxacin moiety.

As shown in Fig. 7F, two clear trends emerge the oxidation current increases from acidic to neutral pH, reaching a maximum at pH 7, and then decreases at higher pH levels. At the same time, the oxidation potential gradually shifts toward more positive values as pH rises. This behavior highlights the critical role of protons in facilitating electron transfer and maintaining redox activity. The peak current at pH 7 confirms it as the most favorable condition for LFX oxidation, consistent with a two-electron, two-proton mechanism. Hence, pH 7 was selected for all subsequent electrochemical experiments.

3.10. Analytical performance of Er_2MoO_6-Temp-2/GCE toward LFX detection

3.10.1. Effect of LFX concentration

To evaluate the electrochemical response of Er_2MoO_6-Temp-2/GCE toward different concentrations of LFX, CV measurements were carried out in 0.1 M PBS (pH 7.0) over a potential range of 0.2–1.4 V at a scan rate of 0.05 $V{\cdot}s^{-1}$. LFX concentration was gradually increased from 50 to 250 μM. As shown in Fig. 8A, the anodic peak current (Ipa) increased consistently with rising LFX levels, indicating strong sensitivity and excellent electrocatalytic activity. This enhancement is attributed to the high conductivity and porous nature of the thermally optimized Er_2MoO_6-Temp-2, which promotes efficient electron transfer. Additionally, π–π stacking interactions between LFX and the electrode surface facilitate better adsorption and faster charge transfer. The consistent increase in Ipa without peak shift or saturation highlights the sensor's stability and responsiveness. Fig. 8B further confirms a strong linear correlation between current and LFX concentration, supporting its suitability for quantitative analysis. The calibration plot of current (Ipa) vs. LFX concentration displayed a good linear fit, as expressed by the linear regression **eq. 6**

$$\boldsymbol{Ipa = 0.0402\,[\mu M] + 0.988, R2 = 0.9977} \quad (6)$$

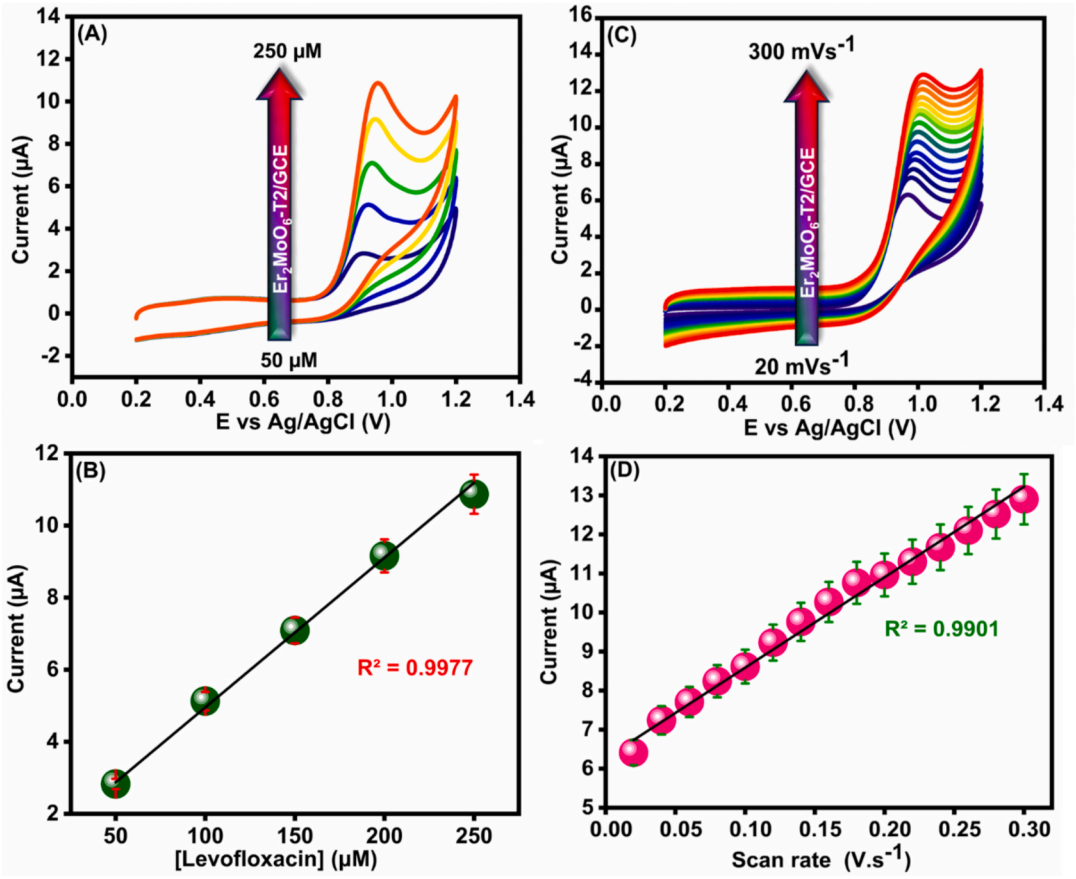

Fig. 8. (A) CV responses of Er_2MoO_6–T2/GCE in 0.1 M PBS containing LFX at concentrations ranging from 50 to 250 μM. (B) Corresponding calibration plot showing the linear relationship between peak current and LFX concentration. (C) CV profiles of Er_2MoO_6–T2/GCE in 50 μM LFX solution at scan rates ranging from 20 to 300 mV/s. (D) Linear plot of peak current versus scan rate, indicating a diffusion-controlled electrochemical process.

3.10.2. Effect of scan rate

The electrochemical behavior and kinetics of the Er_2MoO_6-T2/GCE electrode toward LFX were assessed using CV at scan rates ranging from 20 to 300 mV·s^{-1} in 0.1 M PBS pH 7 containing 100 μM LFX. As shown in Fig. 8C, the anodic peak current (Ipa) increased steadily with scan rate, indicating efficient electro-oxidation and a surface-controlled process. This suggests a strong interaction between LFX and the Er_2MoO_6-modified surface. A slight positive shift in peak potential with scan rate further confirms the irreversibility of the oxidation process, likely influenced by kinetic and mass transport factors. Fig. 8D shows a linear relationship between Ipa and scan rate (ν), with a regression value of $R^2 = 0.996$, supporting an adsorption-controlled mechanism.

3.11. DPV sensing performance, selectivity, operational stability, and reproducibility

3.11.1. Differential pulse voltammetry (DPV) analysis

DPV was used to assess the sensing performance of the Er_2MoO_6–T2-modified electrode due to its high resolution and sensitivity at trace analyte levels. As shown in **Fig. 9 A**, increasing LFX concentrations in 0.1 M phosphate buffer (pH 7) produced a steady rise in peak current without distortion or saturation, indicating efficient electron transfer and strong analyte interaction. **Fig. 9B** shows a clear linear relationship between peak current and LFX concentration across both low and high ranges, with correlation coefficients of 0.9915 and 0.985, respectively. The detection limit (LOD) was calculated to be 0.00146 μM using the standard formula **Eq. 7** [47].

$$LOD = 3*SD/S \quad (7)$$

where s is the slope of the calibration curve and SD is the standard deviation of the blank response.

The enhanced DPV response is linked to the redox-active Er and Mo centers in the Er_2MoO_6 lattice, which provide multiple electron-transfer sites for efficient charge movement. The T2 stabilizes oxidation states and increases the availability of active Mo^{6+}/Mo^{5+} redox couples, enabling faster electron exchange with LFX. Additionally, more surface oxygen vacancies and exposed Mo—O sites improve analyte adsorption and redox activity at the electrode surface. Together, these factors speed up electron tunneling and reduce the energy barrier for redox reactions, boosting peak currents even at very low concentrations. This synergy between surface interaction, redox centers, and defects underpins the high sensitivity and stability of the Er_2MoO_6–T2 sensor, making it promising for precise electrochemical detection and environmental monitoring.

3.11.2. Selectivity, reproducibility, repeatability, and stability evaluation of Er_2MoO_6–T2/GCE sensor

To validate the practical viability of the Er_2MoO_6–T2-modified GCE for LFX sensing, extensive performance metrics, including interference tolerance, reproducibility, repeatability, and long-term stability, were assessed **(Fig. 9C—F).**

Fig. 9C demonstrates the excellent selectivity of the Er_2MoO_6–T2/GCE sensor toward LFX detection, even in the presence of various potentially interfering substances. The analytes tested included nitrofurantoin, nitrobenzene, nitrofurazolidone, dopamine, uric acid, ascorbic acid, glucose, Cd^{2+}, Pb^{2+}, humic acid, and ciprofloxacin, each evaluated at concentrations 10 to 100 times higher than the LFX decision threshold. Remarkably, the oxidation peak current of LFX (~0.88 V) remained almost unchanged, showing signal variations below 4.5 % across all tests. Additionally, the tolerance ratios demonstrated that the sensor maintained accurate detection even under highly challenging conditions. The calculated recovery rates ranged from 95.2 % to 104.1 %, confirming the sensor's robust anti-interference capability. This exceptional selectivity can be attributed to the thermally optimized

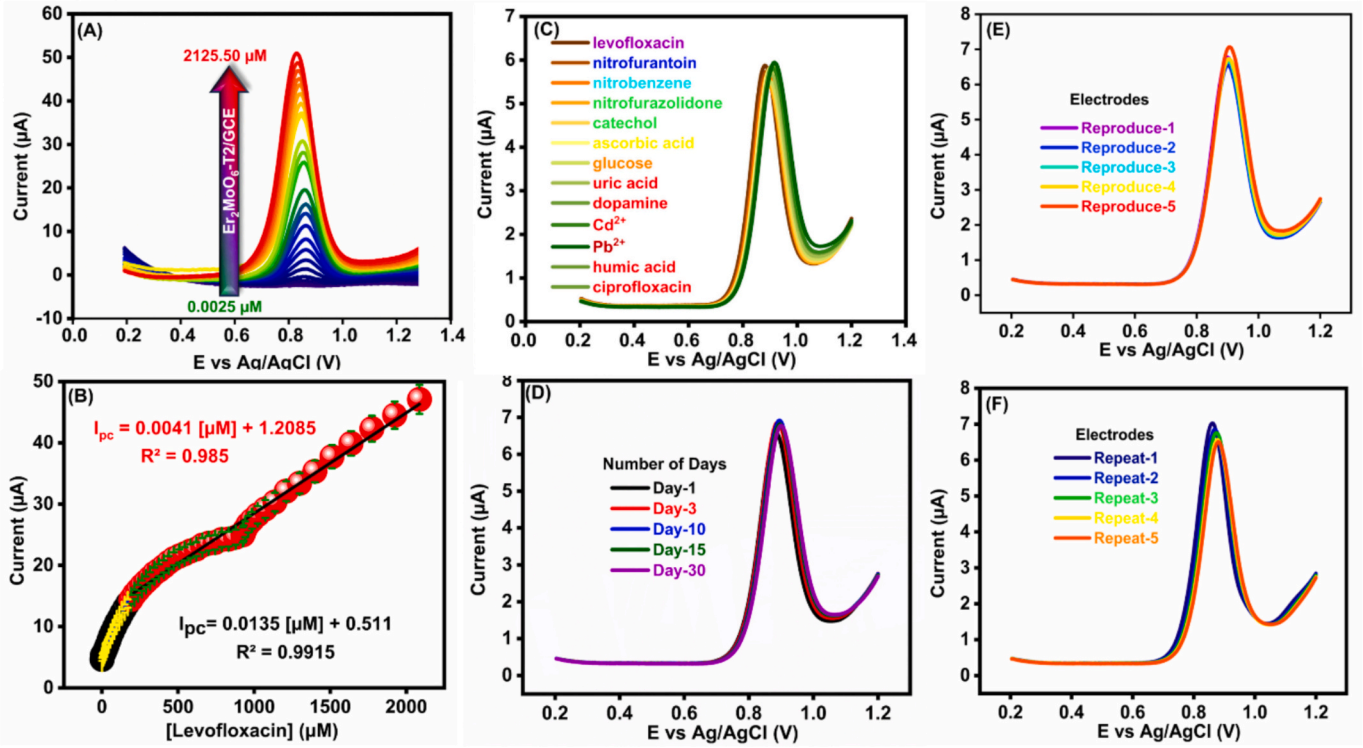

Fig. 9. (A) (DPV) responses of Er_2MoO_6–T2/GCE in the presence of LFX at concentrations ranging from 0.0025 to 2125.50 μM. (B) Calibration plot showing the linear relationship between peak current and LFX concentration. (C) Selectivity analysis of Er_2MoO_6–T2/GCE for LFX detection in the presence of potential interfering substances, including nitrofurantoin, nitrobenzene, nitrofurazolidone, dopamine, uric acid, ascorbic acid, glucose, Cd^{2+}, Pb^{2+}, humic acid, and ciprofloxacin. (D) Stability study of Er_2MoO_6–T2/GCE over multiple days. (E) Reproducibility analysis based on responses from independently prepared Er_2MoO_6–T2/GCE electrodes. (F) Repeatability study assessing the performance of a single Er_2MoO_6–T2/GCE electrode over successive measurements.

Er_2MoO_6–T2 nanostructure, which provides abundant active sites, promotes preferential surface adsorption of LFX molecules, and facilitates efficient electron transfer kinetics, effectively suppressing nonspecific responses from coexisting environmental and biological species.

Reproducibility was evaluated by fabricating five independent Er_2MoO_6–T2-modified electrodes under identical conditions. As shown in Fig. 9**E**, all electrodes produced nearly identical responses to 10 μM LFX, with an average anodic peak current of 6.27 μA and a low relative standard deviation (RSD) of 2.3 %, indicating excellent fabrication consistency. Fig. 9**F** illustrates repeatability, assessed by five consecutive DPV scans on a single modified electrode. The peak current remained stable with minimal deviation RSD = 1.6 %, demonstrating strong adhesion, uniform sensing layer distribution, and durability under continuous use.

Long-term stability was evaluated using freshly prepared Er_2MoO_6–T2/GCE electrodes over a period of five consecutive days Fig. 9**D**. The sensor retained 96.5 % of its initial response, with an RSD of 2.9 %, demonstrating excellent operational and storage stability. To further validate the robustness of the sensor, its performance was also monitored in representative water chemistries, including lake water, pond water, and PBS, where consistent responses were observed without significant performance degradation. Signal drift analysis confirmed a variation of less than 4.5 % across repeated measurements at a fixed LFX concentration, indicating high reproducibility. In addition, the antifouling capability of the electrode was examined by testing biological samples urine and plasma and environmental water matrices. After each measurement, the electrode surface was regenerated by rinsing with PBS/ethanol, successfully restoring over 95 % of the original response, demonstrating excellent regeneration efficacy and fouling resistance. This long-term durability is attributed to the thermal stabilization achieved through high-temperature synthesis, which enhances grain densification, minimizes surface defects, and improves film integrity, enabling reliable and stable sensor performance under real-world conditions. **Table S3** compares this sensor's performance with previously reported electrochemical LFX sensors.

3.12. Real sample preparation

To evaluate the real-world applicability of the Er_2MoO_6–T2-modified electrochemical sensor, its performance was tested using complex biological and environmental samples, including human urine, blood, lake water, and pond water.

Blood samples were collected from healthy adult donors using EDTA-coated vacutainers, and plasma was separated by centrifugation at 4000 rpm for 10 min. The plasma was then diluted 10-fold with 0.1 M phosphate buffer solution (PBS, pH 7.0) to reduce viscosity and minimize matrix interferences. Fresh urine samples were filtered through 0.22 μm syringe filters to remove particulates and diluted 5-fold with PBS to prevent electrode fouling and ensure compatibility with the electrochemical sensor. Environmental water samples from local lakes and ponds in Taiwan were also filtered through 0.22 μm membranes to eliminate suspended solids but were tested without pH adjustment,

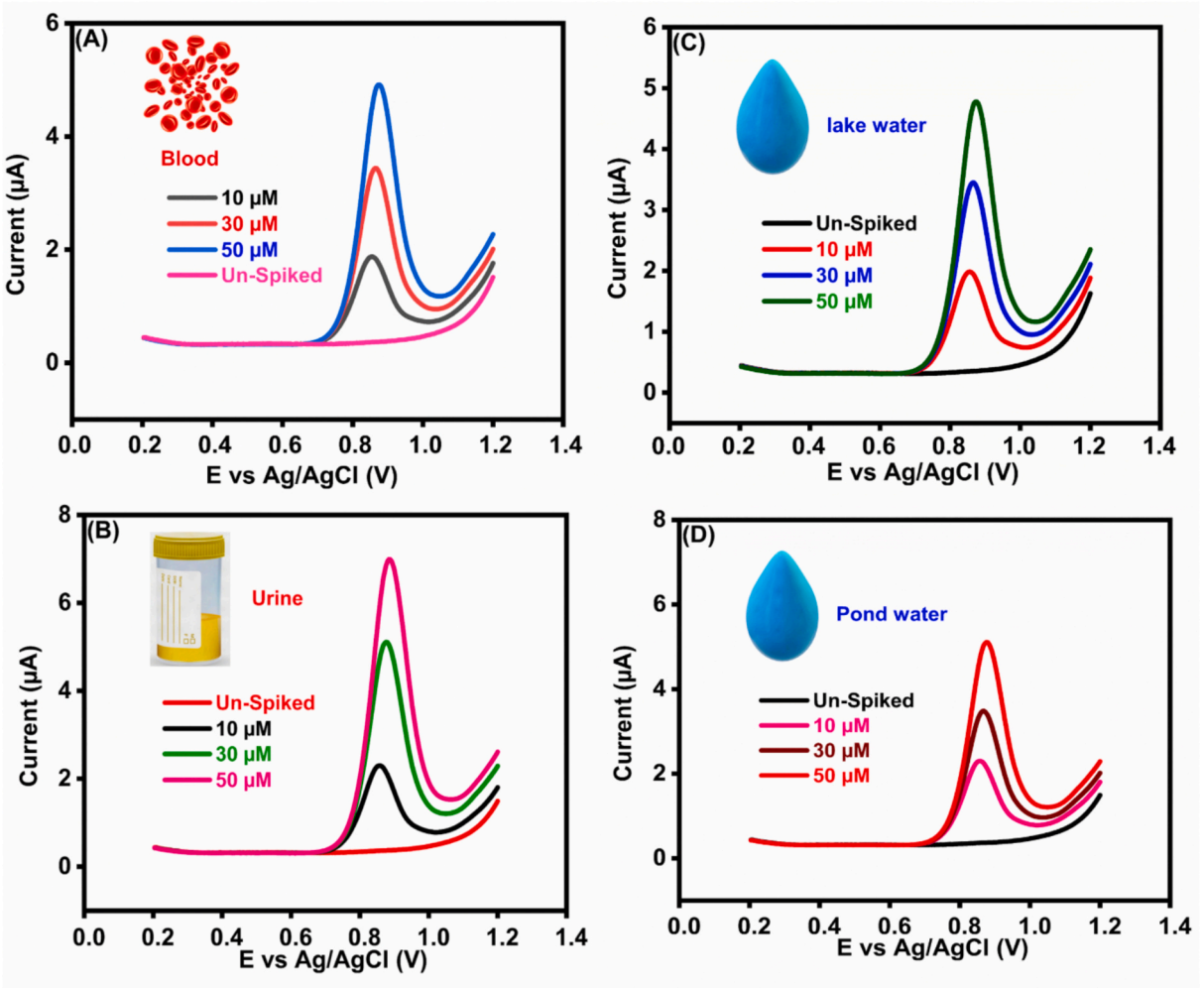

Fig. 10. Real sample analysis using Er_2MoO_6–T2/GCE: (A) DPV responses in blood samples with and without spiked LFX, (B) DPV responses in urine samples with and without spiked LFX, (C) Analysis of LFX in spiked and unspiked lake water samples, and (D) Analysis of LFX in spiked and unspiked pond water samples.

preserving their natural physicochemical conditions. These preparation steps ensured reproducibility and data accuracy while maintaining the integrity of the real samples, enabling a reliable evaluation of the sensor's practical performance.

3.12.1. Real sample evaluation with the Er_2MoO_6–T2-based sensor

The real-sample performance of the Er_2MoO6–T2/GCE was assessed using DPV for the detection of LFX in human urine, blood plasma, lake water, and pond water. To ensure accurate quantification, matrix-matched calibration curves were prepared by spiking known concentrations of LFX (10, 30, and 50 μM) into each real-sample matrix, minimizing matrix effects and improving analytical precision. As shown in Fig. 10A, urine samples exhibited negligible background signals, while clear, concentration-dependent peaks were observed upon LFX spiking, confirming efficient analyte recognition and fast electron transfer. A similar trend was observed for blood plasma Fig. 10B, where clean baselines and well-defined peaks demonstrated the sensor's compatibility with protein-rich biological fluids. For lake and pond water Fig. 10C and D, the sensor maintained linear, stable responses without potential shifts, indicating robust tolerance to environmental matrix interferences.

The recovery results are summarized in **Table S4 (Supplementary Information)** and reported as mean ± standard deviation (SD) along with 95 % confidence intervals (CI), confirming a high average recovery of 98.6 %. No significant signal loss or electrode fouling was observed across repeated measurements, demonstrating the sensor's chemical stability, anti-fouling properties, and strong suitability for practical environmental and biological monitoring.

4. Conclusion

In summary, for the first time, we report temperature-optimized Er_2MoO6 nanostructures for the electrochemical detection of LFX. The improved crystallinity, surface uniformity, and porous flake-like morphology, as confirmed by XRD, Raman, FTIR, SEM, EDS, and XPS, are attributed to the higher thermal energy, which results in enhanced charge transport and increased redox activity. CV, DPV, and EIS analyses demonstrated that the Er_2MoO6–T2-modified electrode follows a two-electron, two-proton oxidation mechanism, exhibiting excellent sensitivity and low charge-transfer resistance. The sensor displayed remarkable signal stability, a wide linear detection range, and high reproducibility in both standard solutions and real-world samples, including human urine, blood plasma, and lake and pond water, achieving recovery rates close to 99 %. Thus, the thermally engineered Er_2MoO6 emerges as an efficient electrode for electrochemical monitoring in environmental systems. Moreover, the temperature-optimized synthesis offers a scalable route to tune rare-earth nanostructures for enhanced performance. This strategy holds significant potential for advanced environmental and biomedical sensing applications.

CRediT authorship contribution statement

Kumar Gokulkumar: Writing – review & editing, Writing – original draft, Investigation, Formal analysis, Data curation, Conceptualization. **Sri Balaji Natarajan:** Writing – review & editing, Writing – original draft, Software, Methodology, Investigation, Formal analysis, Data curation, Conceptualization. **Shen-Ming Chen:** Validation, Supervision, Project administration, Funding acquisition. **Sakthivel Kogularasu:** Writing – review & editing, Data curation. **Shih-Hsuan Chen:** Software. **Kun-Mu Lee:** Validation, Supervision, Project administration, Funding acquisition.

Declaration of competing interest

The authors declare that they have no known competing financial interests or personal relationships that could have appeared to influence the work reported in this paper.

Acknowledgments

This research investigation is supported by the National Science and Technology Council, Taiwan (Grant Number NSTC 111-2223-E-182-001-MY4), Chang Gung University (URRPD2Q0041), Chang Gung Memorial Hospital, Linkou, Taiwan (CMRPD2M0042), and National Taipei University of Technology, Taiwan. (NSTC 114-2113-M-027-008).

Appendix A. Supplementary data

Supplementary data to this article can be found online at https://doi.org/10.1016/j.jwpe.2025.108757.

Data availability

Data will be made available on request.

References

[1] G.-F. Zhang, et al., Ciprofloxacin derivatives and their antibacterial activities, Eur. J. Med. Chem. 146 (2018) 599–612.
[2] M.A. Salam, et al., Antimicrobial resistance: a growing serious threat for global public health, in: Healthcare, 2023, p. 11, 3.
[3] A.I. Samreen, H. Malak, H. Abulreesh, Environmental antimicrobial resistance and its drivers: a potential threat to public health, J Glob Antimicrob Resist 27 (2021) 101–111.
[4] S.M. Wimer, L. Schoonover, M.W. Garrison, Levofloxacin: a therapeutic review, Clin. Ther. 20 (6) (1998) 1049–1070.
[5] A. Lambert, J.-B. Regnouf-de-Vains, M.F. Ruiz-López, Structure of levofloxacin in hydrophilic and hydrophobic media: relationship to its antibacterial properties, Chem. Phys. Lett. 442 (4–6) (2007) 281–284.
[6] N. Wei, et al., Polymorphism of levofloxacin: structure, properties and phase transformation, CrystEngComm 21 (41) (2019) 6196–6207.
[7] D.S. North, D.N. Fish, J.J. Redington, *Levofloxacin, a second-generation fluoroquinolone.* Pharmacotherapy: the journal of human pharmacology and drug, Therapy 18 (5) (1998) 915–935.
[8] D.N. Fish, A.T. Chow, The clinical pharmacokinetics of levofloxacin, Clin. Pharmacokinet. 32 (1997) 101–119.
[9] H.D. Langtry, H.M. Lamb, Levofloxacin: its use in infections of the respiratory tract, skin, soft tissues and urinary tract, Drugs 56 (3) (1998) 487–515.
[10] S.J. Martin, R. Jung, C.G. Garvin, A risk-benefit assessment of levofloxacin in respiratory, skin and skin structure, and urinary tract infections, Drug Saf. 24 (2001) 199–222.
[11] G.J. Noel, A review of levofloxacin for the treatment of bacterial infections, Clinical Medicine. Therapeutics 1 (2009) p. CMT. S28.
[12] V. Okhrits, E. Veliyev, What is the difference between levofloxacin and ofloxacin. Antibiotic ciprofloxacin: description, indications for use and medicinal properties of the drug, Allergy (2020).
[13] T. Kaden, et al., Evaluation of drug-induced liver toxicity of trovafloxacin and levofloxacin in a human microphysiological liver model, Sci. Rep. 13 (1) (2023) 13338.
[14] S. RANJAN, R. Chaitali, S.K. SINHA, *Gas chromatography–mass spectrometry (GC-MS): a comprehensive review of synergistic combinations and their applications in the past two decades.* Journal of analytical sciences and applied, Biotechnology 5 (2) (2023) 72–85.
[15] C. Hao, X. Zhao, P. Yang, GC-MS and HPLC-MS analysis of bioactive pharmaceuticals and personal-care products in environmental matrices, TrAC Trends Anal. Chem. 26 (6) (2007) 569–580.
[16] K. Gokulkumar, et al., Nanoparticles of SnS on carbon nanofibers for electrochemical detection of vanillin, ACS Applied Nano Materials 7 (11) (2024) 13183–13193.
[17] K. Gokulkumar, I.J.D. Priscillal, S.-F. Wang, Deep eutectic solvent-mediated synthesis of PDA coated f-CNF doped ZnS nanoparticles for electrode modification: innovative sensing platform for determination of pollutant 3-nitrophenol, J. Alloys Compd. 924 (2022) 166561.
[18] K. Gokulkumar, et al., Enhanced electrochemical detection of tartrazine in beverages and liquid soap via nickel phosphide-adorned functionalized carbon nanofibers, J. Taiwan Inst. Chem. Eng. 157 (2024) 105420.
[19] B. Sriram, et al., Designing of highly active hexagonal α-zirconium phosphate nanoparticles decorated halloysite nanotube composite for voltammetry sensing of azomycin drug, Chem. Eng. J. 509 (2025) 161220.
[20] I. da Silva, et al., Solid-state synthesis and phase transitions in the RE2 (MoO4) 3 family monitored by thermodiffraction, Cryst. Growth Des. 23 (4) (2023) 2417–2429.
[21] X. Liu, et al., Rare earth erbium molybdate nanoflakes decorated functionalized carbon nanofibers: an affordable and potential catalytic platform for the electrooxidation of phenothiazine, Electrochim. Acta 358 (2020) 136885.

[22] G. Tan, L.-D. Zhao, M.G. Kanatzidis, Rationally designing high-performance bulk thermoelectric materials, Chem. Rev. 116 (19) (2016) 12123–12149.
[23] H. Hamdi, H.R. Abedi, Y. Zhang, A review study on thermal stability of high entropy alloys: Normal/abnormal resistance of grain growth, J. Alloys Compd. 960 (2023) 170826.
[24] Y. Zhang, et al., Inhibition of crystal nucleation and growth: a review, Cryst. Growth Des. 24 (6) (2024) 2645–2665.
[25] K.-J. Wu, et al., Nucleation and growth in solution synthesis of nanostructures–from fundamentals to advanced applications, Prog. Mater. Sci. 123 (2022) 100821.
[26] W. Yao, B. Wu, Y. Liu, Growth and grain boundaries in 2D materials, ACS Nano 14 (8) (2020) 9320–9346.
[27] X.-L. Shi, J. Zou, Z.-G. Chen, Advanced thermoelectric design: from materials and structures to devices, Chem. Rev. 120 (15) (2020) 7399–7515.
[28] N.-C. Godja, F.-D. Munteanu, Hybrid nanomaterials: a brief overview of versatile solutions for sensor technology in healthcare and environmental applications, Biosensors 14 (2) (2024) 67.
[29] P. Kannan, G. Maduraiveeran, Metal oxides nanomaterials and nanocomposite-based electrochemical sensors for healthcare applications, Biosensors 13 (5) (2023) 542.
[30] Z.U. Abideen, W.U. Arifeen, Y.N.D. Bandara, Emerging trends in metal oxide-based electronic noses for healthcare applications: a review, Nanoscale 16 (19) (2024) 9259–9283.
[31] S. Kogularasu, et al., 3D graphene oxide-cobalt oxide polyhedrons for highly sensitive non-enzymatic electrochemical determination of hydrogen peroxide, Sensors Actuators B Chem. 253 (2017) 773–783.
[32] Y.-Y. Lee, et al., Eco-innovative electrochemical sensing for precise detection of vanillin and sulfadiazine additives in confectioneries, Appl Surf Sci Adv 20 (2024) 100584.
[33] S. Kogularasu, et al., A novel synthesis of nickel carbide modified glassy carbon electrode for electrochemical investigation of archetypal diabetes biomarker in human serum and urine samples, J. Electrochem. Soc. 171 (4) (2024) 047512.
[34] B. Sriram, et al., The fabrication of a La2Sn2O7/f-HNT composite for non-enzymatic electrochemical detection of 3-nitro-l-tyrosine in biological samples, Biosensors 13 (7) (2023) 722.
[35] J. Sun, et al., A single-atom manganese nanozyme mediated membrane reactor for water decontamination, Water Res. 268 (2025) 122627.
[36] H. Wang, et al., Photothermal nano-confinement reactor with bimetallic sites for enhanced peroxymonosulfate activation in antibiotic degradation, Water Res. 268 (2025) 122623.
[37] Y. Zhao, et al., Electrified ceramic membrane actuates non-radical mediated peroxymonosulfate activation for highly efficient water decontamination, Water Res. 225 (2022) 119140.
[38] B. Sriram, et al., Deep eutectic solvent-mediated synthesis of spinel zinc chromite nanoparticles: a simple label-free electrochemical sensor for dopamine and ascorbic acid, ACS Applied Nano Materials 6 (19) (2023) 17593–17602.
[39] S. Kogularasu, et al., Sea-urchin-like Bi2S3 microstructures decorated with graphitic carbon nitride nanosheets for use in food preservation, ACS Applied Nano Materials 5 (2) (2022) 2375–2384.
[40] M. Gallagher, Penn State University, University Park, PA, USA, ICDD Grant-in-Aid, 1973.
[41] P. Wang, et al., Structural and cryogenic magnetic properties of the RE2MoO6 (RE= Er and ho) compounds, Ceram. Int. 49 (5) (2023) 8508–8515.
[42] H. Nakano, N. Kamegashira, Microstructure of a complex oxide, Er2Mn2/3Mo4/3O7, with a Pyrochlore-related structure, J. Am. Ceram. Soc. 84 (6) (2001) 1374–1378.
[43] M.R. Joya, J. Alfonso, L. Moreno, Photoluminescence and Raman studies of α-MoO_3 doped with erbium and neodymium, Curr. Sci. 116 (10) (2019) 1690–1695.
[44] J. Lin, et al., Expansion of the structural diversity of f-element bearing molybdate iodates: synthesis, structures, and optical properties, Dalton Trans. 48 (15) (2019) 4823–4829.
[45] B. Binish, et al., Defect state enhanced nonlinear absorption and optical limiting behaviour of erbium doped silver molybdate nanostructures, Sci. Rep. 15 (1) (2025) 2615.
[46] K. Alagumalai, et al., Development of AgVO3/PPy/N@ rGO composite sensor for efficient electrochemical monitoring of levofloxacin in human fluids and environmental samples, Colloids Surf. A Physicochem. Eng. Asp. 706 (2025) 135791.
[47] M. Govindaraj, et al., Surfactant-assisted synthesis of metallic-ag/nickel oxide on graphitic carbon nitride composite: an electrochemical investigation of synthetic vanillin, ACS Appl. Mater. Interfaces. 17 (7) (2025) 11287–11299.